Phase-contrast x-ray imaging with a liquid-metal-jet-anode microfocus source

T. Tuohimaa, M. Otendal, and H. M. Hertz[a)]
*Biomedical and X-Ray Physics, Department of Applied Physics, KTH Royal Institute of Technology/
Albanova, SE-10691 Stockholm, Sweden*

Phase-contrast methods increase contrast, detail, and selectivity in x-ray imaging. Present compact x-ray sources do not provide the necessary spatial coherence with sufficient power to allow the laboratory-scale high-resolution phase-contrast imaging with adequate exposure times. In this letter, the authors demonstrate phase-contrast imaging with few-micron detail employing a compact ~6.5 μm spot liquid-metal-jet-anode high-brightness microfocus source. The 40 W source is operated at more than ten times higher electron-beam power density than present microfocus sources and is shown to provide sufficient spatial coherence as well as scalability to high power, thereby enabling the application of phase-contrast x-ray imaging with short exposure times in clinics and laboratories. © 2007 American Institute of Physics. [DOI: 10.1063/1.2769760]

Insufficient natural absorption contrast often limits the image quality in classical x-ray imaging such as medical radiography and nondestructive testing.[1] Phase-shift measurements[2–4] may provide improved contrast since the real (phase) part δ of the refractive index $(1-\delta-i\beta)$ is several orders of magnitude higher than the imaginary (absorption) part β. Typically, δ/β is larger than 10^3 at 20 keV in carbon-oxygen compounds such as, e.g., soft tissue or plastics, resulting in improved imaging of and discrimination between tissue or structures with low and/or similar absorption[4,5] Higher contrast also increases the observable spatial resolution. Thus, phase-contrast imaging has potential to become an important high-resolution and high-contrast imaging tool provided it can be performed with adequate exposure times in the laboratory or clinic.

Phase-contrast x-ray imaging can be performed either directly (interferometry) or indirectly via the gradient (e.g., in-line holography or diffraction-enhanced imaging).[4] The key issue for phase-contrast imaging is that the emitted radiation field has sufficient spatial coherence; i.e., the source should have a small apparent angular size.[6] This may be achieved either by having a small source at close distance or a larger source at long distance from the object. Thus, high-brightness sources [where brightness is proportional to photons/$(s \times \mu m^2 \times sr)$] have an advantage and, consequently, phase imaging has primarily been performed at synchrotron sources.[4,5] Such studies have shown significantly enhanced contrast over conventional methods, revealing soft tissue discrimination of diagnostic importance in, e.g., cartilage, lungs, and breast tissue.[4,5] Phase-contrast imaging has also been demonstrated with compact electron-impact sources, both directly with polychromatic x-rays from a microfocus source[6] and in combination with a crystal monochromator.[7] Unfortunately, the power of presently available compact sources with sufficient brightness is too low to perform clinical- or laboratory-scale phase-contrast imaging with adequate exposure times. Since the vast majority of present x-ray imaging is performed with compact sources at small-scale facilities, this prevents the widespread use of phase-contrast imaging in medical and nonmedical applications.

In the present letter, we demonstrate high-resolution in-line holography of weakly absorbing objects with a compact electron-impact x-ray microfocus source. This liquid-metal-jet-anode microfocus source[8] can be operated at high brightness and may be scaled to high power, thereby allowing examinations with short exposure times. The brightness of electron-impact x-ray sources scales with the electron-beam power density on the anode and is limited by e-beam-induced thermal damage to the anode.[1] For microfocus x-ray tubes with circular foci (typically less than few tens of microns in diameter), the maximum e-beam power loading is in the range of 0.4–0.8 W per electron-beam diameter in micrometers [full width at half maximum (FWHM) of Gaussian beam].[9] This corresponds to an e-beam power density at the anode of approximately $25-50 \text{ kW/mm}^2$ for a 10 μm source. For comparison, sources with large spots typically operate in the $1-20 \text{ kW/mm}^2$ range, where the lower end applies to stationary anodes and the higher end relates to short exposures with rotating-anode sources. Angled viewing of a line focus can increase the apparent, but not the actual, power density for large-spot geometries. Due to the thermal limitations, it is difficult to envision any significant further increase in maximum e-beam power density for conventional anode technology.[10,11] We employ a liquid-tin jet as the anode, as shown in Fig. 1. This electron-impact microfocus source shows promise for high-power operation with two to three orders of magnitude higher e-beam power density than present electron-impact sources.[12] Briefly, this increase in e-beam power density limit is due to a high speed of the metal-jet anode and the thermal properties and regenerative nature of the liquid-jet anode.[12,13]

Figure 1 depicts the experimental arrangement. The x-ray source with its electron gun, liquid-tin-jet anode, and tin heating arrangement are placed in a vacuum chamber while the objects to be imaged and detectors are outside the chamber. The tin is radiation heated in a high-pressure vessel to ~300 °C. By applying ~80 bars of nitrogen pressure, a stable ~35 m/s, 30 μm diameter liquid-tin jet is injected into the vacuum chamber via a tapered glass nozzle. The
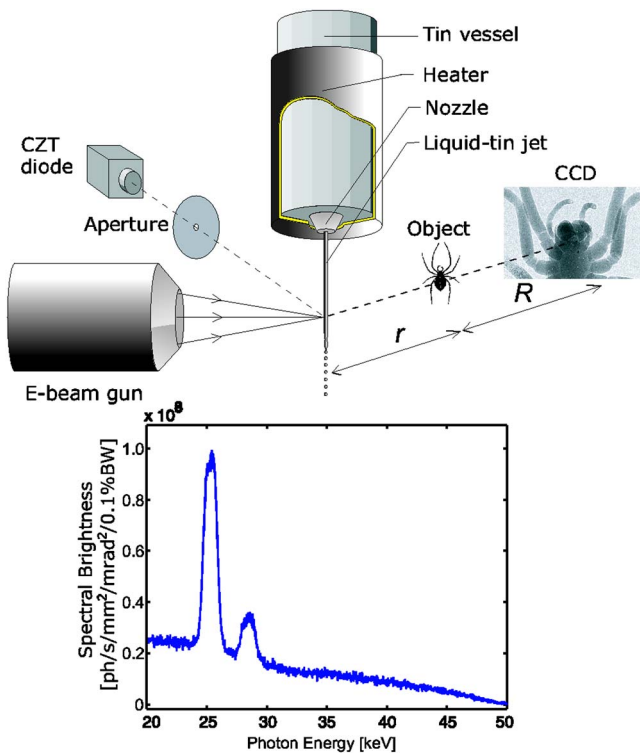
a)Electronic mail: hans.hertz@biox.kth.se

FIG. 1. Experimental arrangement of the x-ray phase-contrast imaging system with its electron-impact liquid-tin-jet-anode source.
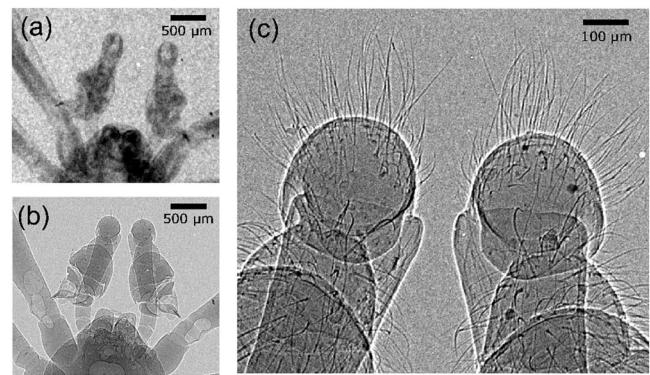

FIG. 2. (a) Absorption image of a spider. The exposure time is $T=30$ s and the magnification is $M=1$ ($r=51$ cm and $R=0.5$ cm). (b) Phase-contrast imaging of the spider ($T=15$ s, $M=3.4$, $r=15$ cm, and $R=36$ cm). (c) Detail at higher magnification showing part of the pedipalps ($T=30$ s, $M=8.5$, $r=15$ cm, and $R=112$ cm).

50 kV LaB$_6$-cathode e-beam is focused by a magnetic lens onto the liquid-tin jet, resulting in a high-brightness x-ray spot. An x-ray charge coupled device detector used for imaging and a calibrated CdZnTe diode for spectral flux measurements operate at 90° to the e-beam. Together with source size measurements, this gives calibrated spectral brightness data.

In the present experiments, the source is typically operated at 40 W e-beam power. The Gaussian e-beam diameter (FWHM) is estimated to be $4-5$ μm from simulations.[14] Thus, the source operates at >8 W/μm e-beam power loading, corresponding to approximately 1 MW/mm^2 e-beam power density at the anode. The x-ray spot size is determined via deconvolution of an edge in the image of a 20 μm thick gold edge, resulting in a source diameter of ~6.5 μm FWHM. The x-ray spot is larger than the e-beam spot for microfocus sources due to, e.g., electron scattering in the anode material. Thus, the experimentally determined x-ray brightness expressed in e-beam power per x-ray spot size is ~600 kW/mm^2 without any angled-viewing enhancement. The inset in Fig. 1 shows the calibrated spectrum. In addition to the broad bremsstrahlung emission, there are two prominent peaks due to Sn K_α and K_β emission at 25.3 and 28.5 keV, respectively. The bremsstrahlung and peak spectral brightness in Fig. 1 are 2.5×10^7 and 1.0×10^8 photons/(s μm^2 sr 0.1% bandwidth), respectively. The actual spectral brightness of the ~12 eV wide $K\alpha$ doublet peak[15] is >65 times higher than in the figure due to the 1.2 keV spectral bandwidth of the CdZnTe diode at 25 keV.

Figure 2 shows absorption and phase imaging of our test object, a spider. The source-object distance and the object-detector distance are denoted as r and R, respectively, in Fig. 1. The distances vary between each experiment depending on the magnification $[M=(r+R)/r]$ and the degree of

phase contrast desired. Figure 2(a) shows an absorption image ($M=1$, $r=51$ cm, and $R=0.5$ cm). Here structures down to ~200 μm are visible but the limited contrast effectively reduces the observable resolution. Figure 2(b) shows a phase-contrast image with low magnification ($M=3.4$, $r=15$ cm, and $R=36$ cm). The contrast is significantly improved and, in addition, the observable resolution increases resulting in a much more detailed image of the spider. Figure 2(c) shows part of the pedipalps in larger magnification ($M=8.5$, $r=15$ cm, and $R=112$ cm). Note the hair on the pedipalps. This thin hair was measured to 10 μm at the base and a few microns at the top with an optical microscope. Thus, phase contrast not only increases contrast but also effectively increases the observable resolution. The exposure time was 15 s in Fig. 2(b) and 30 s in Fig. 2(c). Thus, already with the present low-power proof-of-principle version of the liquid-metal-jet source, the typical exposure times are more than an order of magnitude shorter than in previous work based on compact electron-impact sources.[6]

Figure 3(a) shows the phase-contrast image of nominally 10, 25, 45, and 130 μm diameter latex beads ($M=5.8$, $r=25$ cm, and $R=120$ cm). Phase effects provide edge enhancement and overall increased contrast resulting in that the beads are clearly visible. In comparative absorption images, the beads are not detectable. For example, the absorption at 25 keV for 130 and 25 μm beads is 0.5% and 0.1%, respec-
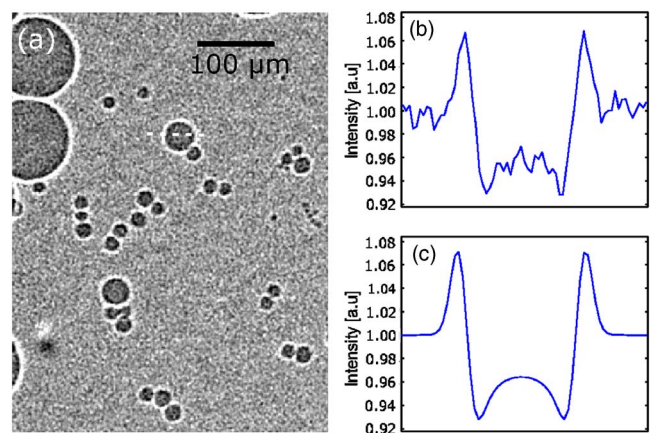

FIG. 3. (a) Phase image of latex beads with different sizes ($T=180$ s, $M=5.8$, $r=25$ cm, and $R=120$ cm). (b) Line scan across a 45 μm diameter bead. (c) Wave-propagation simulation of the imaging of the 45 μm bead.

tively. Figure 3(b) shows the one-dimensional intensity profile of a 45 μm bead and compares it with a theoretically modeled intensity profile [Fig. 3(c)]. The model calculates the point-source image with a wave-propagation algorithm in the paraxial regime which is based on the Fresnel-Kirchoff integral and Fourier-transform methods.[16] Refractive index data (δ, β) are taken from Ref. 17. The simulated point-source image is then convolved with Gaussian point-spread functions of the source (6.5 μm FWHM) and detector (35 μm FWHM) and finally integrated over the spectral distribution of the source. The convolution decreases the contrast of the interference fringes and models the effect of the finite spatial coherence length $d_s = \lambda / \gamma$, where λ is the wavelength and γ is the angular width of the source.[6] For 25 keV x-rays and our 6.5 μm source d_s is ~8 μm at 1 m distance from the source. The spectral integration is a first-order approximation of the effect on the image of the limited temporal coherence of the x-ray source. It reduces contrast slightly and is not as crucial to in-line holography as the spatial coherence. The correspondence between the simulated model and the experiments is good. Thus, it is possible to model the contrast for a wide range of objects in our experimental arrangement and use the model for improved image analysis. Based on the experiments and the model, we conclude that both one-dimensional (spider hair) and two-dimensional (beads) objects as small as a few microns are observable with good contrast. Thus, there is potential to observe very weak and small phase objects with high spatial resolution with the liquid-metal-jet-anode source.

Phase imaging has demonstrated greatly enhanced contrast over conventional methods, providing soft tissue discrimination at micron-scale resolution. In addition, it often requires lower dose than absorption imaging due to the better contrast.[4] For widespread clinical or laboratory use, however, it requires a compact x-ray source which provides the necessary spatial coherence in combination with sufficient power. Calculations and experiments show that the x-ray power of the liquid-metal-jet-anode source can be increased at least two orders of magnitude (to several kW:s). The increase primarily relies on higher jet speed[13] and the regenerative nature of the liquid-jet anode which allows thermal damage of the anode.[12,18] Thereby the power would approach that of present large-spot (0.3–0.4 mm) mammography tubes while still operating in the microfocus regime. Thus, the liquid-metal-jet-anode electron-impact source shows promise for microfocus operation at high power and with sufficient spatial coherence to allow routine phase imaging with adequate exposure times.

Several areas would benefit from laboratory-scale phase-contrast imaging. In medical x-ray imaging, better contrast and higher spatial resolution have potential to become important for improved and earlier diagnosis in, e.g., breast, lungs, cartilage, bone, and blood vessels.[4,5,7] The present tin-jet source is suitable for mammography due to its line emission around 25 keV. For medical imaging of thicker objects, Bi or Pb may be suitable anode-jet liquids due to their emission lines around 70–80 keV. Improved resolution and contrast are equally important in nonmedical x-ray applications, e.g., nondestructive testing (NDT) and diffraction. We note that the liquid-metal-jet-anode source performance already exceeds present NDT microfocus tubes and, thus, would reduce exposure time and/or improve contrast in traditional inspection applications. Furthermore, with a high-brightness source based on a liquid-gallium-jet anode[19] (K_α at 9.2 keV), in-house medium-resolution diffraction imaging of biological and other materials is feasible. For these applications, the regenerative nature of the liquid-jet anode is an additional advantage compared to conventional sources since it allows long continuous exposures at peak brightness and power. In summary, the small-spot/high-power liquid-metal-jet-anode microfocus source has potential to enable widespread use of high-resolution and high-contrast phase-contrast imaging.

[1] E. Krestel, *Imaging Systems for Medical Diagnostics* (Siemens, Berlin, 1990).
[2] T. J. Davis, D. Gao, T. E. Gureyev, A. W. Stevenson, and S. W. Wilkins, Nature (London) **373**, 595 (1995).
[3] R. Fitzgerald, Phys. Today **53**(7), 23 (2000).
[4] R. A. Lewis, Phys. Med. Biol. **49**, 3573 (2004).
[5] F. Arfelli, V. Bonvicini, A. Bravin, G. Cantatore, E. Castelli, L. D. Palma, M. D. Michiel, M. Fabrizioli, R. Longo, R. H. Menk, A. Olivo, S. Pani, D. Pontoni, P. Poropat, M. Prest, A. Rashevsky, M. Ratti, L. Rigon, G. Tromba, A. Vacchi, E. Vallazza, and F. Zanconati, Radiology **215**, 286 (2000).
[6] S. W. Wilkins, T. E. Gureyev, D. Gao, A. Pogany, and A. W. Stevenson, Nature (London) **384**, 335 (1996).
[7] V. N. Ingal, E. A. Beliaevskaya, A. P. Brianskaya, and R. D. Merkurieva, Phys. Med. Biol. **43**, 2555 (1998).
[8] O. Hemberg, M. Otendal, and H. M. Hertz, Appl. Phys. Lett. **83**, 1483 (2003).
[9] D. E. Grider, A. Wright, and P. K. Ausburn, J. Phys. D **19**, 2281 (1986).
[10] E. Ammann and W. Kutschera, Br. J. Radiol. **70**, S1 (1997).
[11] J. Freudenberger, E. Hell, and W. Knüpfer, Nucl. Instrum. Methods Phys. Res. A **466**, 99 (2001).
[12] O. Hemberg, M. Otendal, and H. M. Hertz, Optim. Eng. **43**, 1682 (2004).
[13] M. Otendal, O. Hemberg, T. T. Tuohimaa, and H. M. Hertz, Exp. Fluids **39**, 799 (2005).
[14] LORENTZ 2EM, www.integratedsoft.com
[15] Y. Izumi, H. Nagamori, F. Kiyotaki, D. Masih, T. Minato, E. Roisin, J.-P. Candy, H. Tanida, and T. Uruga, Anal. Chem. **77**, 6969 (2005).
[16] J. W. Goodman, *Introduction to Fourier Optics*, 2nd ed. (McGraw-Hill, Singapore, 1996), pp. 66–67.
[17] E. Gullikson, http://www-cxro.lbl.gov/
[18] M. Otendal, T. Tuohimaa, and H. M. Hertz, J. Appl. Phys. **101**, 026102 (2007).
[19] M. Otendal, T. Tuohimaa, U. Vogt, and H. M. Hertz (unpublished).